

# WKGM: Weight-K-space Generative Model for Parallel Imaging Reconstruction

Zongjiang Tu, Die Liu, Xiaoqing Wang, Chen Jiang, Minghui Zhang,  
Qiegen Liu, *Senior Member, IEEE*, Dong Liang, *Senior Member, IEEE*

**Abstract**—Parallel Imaging (PI) is one of the most important and successful developments in accelerating magnetic resonance imaging (MRI). Recently deep learning PI has emerged as an effective technique to accelerate MRI. Nevertheless, most approaches have so far been based image domain. In this work, we propose to explore the k-space domain via robust generative modeling for flexible PI reconstruction, coined weight-k-space generative model (WKGM). Specifically, WKGM is a generalized k-space domain model, where the k-space weighting technology and high-dimensional space strategy are efficiently incorporated for score-based generative model training, resulting in good and robust reconstruction. In addition, WKGM is flexible and thus can synergistically combine various traditional k-space PI models, generating learning-based priors to produce high-fidelity reconstructions. Experimental results on datasets with varying sampling patterns and acceleration factors demonstrate that WKGM can attain state-of-the-art reconstruction results under the well-learned k-space generative prior.

**Index Terms**—Parallel imaging, weight-k-space domain, generative model, scored-based network.

## I. INTRODUCTION

Most approaches undersample data acquisition in k-space to accelerate MRI. Due to the violation of the Nyquist sampling theorem, undersampling in k-space introduces aliasing artefacts. Parallel imaging (PI) [1]-[3] techniques have the ability of reconstructing uncorrupted images from undersampled measurements, with the aid of multi-channel receive coils.

PI reconstruction methods can be classified broadly into two main types depending on the way in which they utilize the coil sensitivity information. Techniques such as Sensitivity Encoding (SENSE) [2], explicitly require sensitivity information for reconstruction. Theoretically, SENSE leverages the acquired sensitivity information of multiple receiving coils to remove aliasing artifacts. In practice, it is often very difficult to accurately and robustly obtain the coil sensitivity information. Another type, such as generalized autocalibrating partially parallel acquisitions (GRAPPA) [3], implicitly uses sensitivity information for reconstruction. Concretely, GRAPPA estimates the coil sensitivity information from additional k-space data, the so-called auto calibration signals (ACSs), and thus reduces side effects brought

by the difficult and inaccurate sensitivity map estimation. Some other autocalibrating methods are, namely, Iterative Self-consistent Parallel Imaging Reconstruction (SPIRiT) [4], auto-calibrated k-space sparse matrix (kSPA) [5], and efficient eigenvector based SPIRiT (ESPIRiT) [6]. However, once the number of acquired ACS is limited, the accuracy of estimated sensitivity maps or kernels decreases, resulting in reconstruction errors. With regard to this issue, calibration-less methods that do not require specific ACS have been proposed. Selecting examples include Calibration-less Multi-coil MRI (CaLM MRI) [7], simultaneous autocalibrating and k-space estimation (SAKE);[8] parallel-imaging low-rank matrix modeling of local k-space neighborhoods (P-LORAKS) [9] and annihilating filter-based low-rank Hankel matrix approach (ALPHA) [10]. Although promising, these reconstructions usually need much more computation for the iterative reconstruction, necessitating new methods that obviate these limitations.

Deep learning methods perform superfast online reconstruction with the aid of offline training using enormous data. While the most existing deep learning MRI researches start from the image domain, few start from the k-space domain. For image domain-based approaches, Hammernik *et al.* [11] designed a Variational Network (VN)-based method to improve multi-channel MRI reconstruction. Schlemper *et al.* [12] proposed a framework for MRI reconstruction using a deep cascade of convolutional neural network to accelerate the data acquisition. Aggarwal *et al.* [13] developed a model-based deep learning architecture to achieve PI, called MoDL. Duan *et al.* [14] introduced a variable splitting network (VS-Net) to efficiently reconstruct the undersampled MR images. Liu *et al.* [15] presented a sparse operator-enhanced iterative network (IFR-Net) for fast CS-MRI reconstruction. Regarding the k-space domain-based methods, inspired by a link between the ALPHA and deep learning, Han *et al.* [16] showed a fully data-driven deep learning algorithm for k-space interpolation. It is a supervised learning technique that requires a great number of paired data for network training.

Recent years generative models have seen remarkable advance. Deep generative models have the advantages of alleviating the deficiency of learning flexibility. In 2014, Goodfellow *et al.* [17] first designed the generative adversarial networks (GANs). Then, various improved GAN models were proposed, which achieved superior performance in MRI. However, the training of GANs can be unstable due to the adversarial training procedure. Score-based generative models (SGMs) [18]-[20] and denoising diffusion probabilistic models (DDPMs) [21]-[22] have gained remarkably success as an emerging class of generative models that have proven promising sample quality without requiring adversarial training. For instance, in the seminal work [23], Song *et al.* proposed a score-based diffusion model by looking at the stochastic differential equation (SDE) associated with the inference process. Soon after, they applied the above technique to medical image reconstruction [24]. Similarly, Quan *et al.* [25] presented HGGDP for MRI reconstruction by taking advantage of the denoising

---

This work was supported in part by National Natural Science Foundation of China under 61871206. (Corresponding authors: Q. Liu and D. Liang)

Z. Tu, D. Liu, C. Jiang, Q. Liu and M. Zhang are with School of Information Engineering, Nanchang University, Nanchang 330031, China. ({tuzongjiang, liudie, jiangchen}@email.ncu.edu.cn, {zhangminghui, liuqiegen}@ncu.edu.cn)

X. Wang is with the institute of Biomedical Imaging, Graz University of Technology, 8010, Graz, Austria. (xiaoqingwang2010@gmail.com).

D. Liang is with Paul C. Lauterbur Research Center for Biomedical Imaging, SIAT, Chinese Academy of Sciences, Shenzhen 518055, China. (dong.liang@siat.ac.cn)

score matching. By leveraging the learned score function as a prior, Chung *et al.* [26] introduced a score-POCS model for solving inverse problems in imaging. Moreover, Jalal *et al.* [27] trained a generative prior for MRI reconstruction. Different from the above-mentioned MRI reconstruction algorithms which are mainly based on the image domain, Xie *et al.* [28] proposed a k-space domain measurement-conditioned denoising diffusion probabilistic model (MC-DDPM) for MRI reconstruction. However, it is conditioned on specific sampling strategy. In this work, we propose a weighted k-space generative model (WKGM) that jointly explores the k-space domain via robust generative modeling for flexible MRI reconstruction.

More detailly, we train an unsupervised score-based model on weighted and high-dimensional k-space data, where weighting technology and high-dimensional space strategy are applied to the initial k-space data for better capturing prior distribution. In the reconstruction stage, we employ Predictor-Corrector (PC) sample as a numerical SDE solver to generate samples and embed data consistency operation. In particular, the reconstruction architecture can integrate any traditional iterative algorithms (e.g., SAKE) into the iterative reconstruction process, generating higher quality reconstructions. We highlight our main contributions as follows:

- **Robust Generative Modeling:** The generative model is learned and generated from the weighted k-space data, neither in the original k-space data nor in the image domain. This strategy leverages the model generalization capability and robustness, i.e., a model that generated from only one coil can be applied to the reconstruction task of any coils, without much performance compromise.
- **Flexible Reconstruction Scheme:** The generative model is utilized in the k-space domain reconstruction procedure with iterative formulation. Therefore, any traditional k-space domain reconstruction methods can be incorporated into the whole reconstruction procedure with flexible forms.

The remainder of this paper is organized as follows. Section II briefly reviews some related PI methods in k-space domain and the research of generative models especially SGMs. In Section III, we first introduce the skeleton of WKGM and then we elaborate on the motivation for using the weighted technique and high-dimensional strategy on k-space data. Additionally, we describe the prior learning and iterative reconstruction process of WKGM in detail. Finally, we introduce the combination of WKGM and traditional algorithm. Section IV presents the MRI reconstruction performance of the proposed method. Section V concludes our findings in this work.

## II. RELATED WORK

### A. Priors in k-Space PI

The observation acquisition forward model for the multi-coil parallel MRI reconstruction problem in k-space domain can be described as follows:

$$y_c = Mk_c + n_c, \quad c = 1, 2, \dots, C \quad (1)$$

where  $M$  is a linear operator that relates reconstructed k-space data  $k = [k_1, \dots, k_c]$  to acquired data  $y = [y_1, \dots, y_c]$ ,  $n_c$  is the noise.  $k_c$  represents the  $c$ -th coil k-space data and  $y_c$  denotes the corresponding acquired k-space measurement data. The PI recovery can be formulated as an optimization problem:

$$\text{Min}_k \|Mk - y\|_2^2 + \lambda R(k) \quad (2)$$

where  $\|Mk - y\|_2^2 = \sum_{c=1}^C \|Mk_c - y_c\|_2^2$  is the data fidelity term,  $\|\cdot\|_2^2$  represents the  $l_2$ -norm,  $C$  denotes the number of coils.  $R(k)$  is the regularization term of  $k_c$ , and  $\lambda$  is the factor that balances the data-fidelity term and the regularization term.

Until now, there exists a large member of algorithms to tackle Eq. (2). For instance, Haldar developed a framework for constrained image reconstruction that used low-rank matrix modeling of local k-space neighborhoods (LORAKS) [29]. Cheng *et al.* [30] developed an approach for image reconstruction with deep neural networks being applied to patches of data in the frequency domain. Based on previous works, Akcakaya *et al.* [31] further put forward a robust artificial-neural-networks for k-space interpolation (RAKI) that is trained on autocalibration signal data. Meanwhile, Kim *et al.* [32] proposed a similar approach, but used a recurrent neural network model named LORAKI. Also, Arefeen *et al.* [33] designed a scan-specific model (SPARK) that estimated and corrected k-space errors made when reconstructing accelerated MR data. Extensive numerical experiments show that their proposed methods consistently outperform the existing image domain deep learning approaches.

### B. Generative Models for MRI Reconstruction

Deep generative models have shown the ability to produce high fidelity results in MRI reconstruction with different strategies. For example, Tezcan *et al.* [34] utilized the variational autoencoders (VAEs) as a tool for describing the data density prior. In the follow-up development, many researchers continued to carry out further research on the basis. Liu *et al.* [35] leveraged a denoising autoencoding (DAE) network as an explicit prior to addressing the highly under-sampling MRI reconstruction problem. In [36], Bora *et al.* presented an algorithm that used generative adversarial network (GAN) for compressed sensing. Autoregressive generative models like PixelCNN have also been verified in MRI reconstruction [37]. In addition, a new generative flow (Glow) [38] formulated in the latent space of invertible neural network-based generative models was proposed for reconstructing MR images. More recently, by using energy function as the generative model, Guan *et al.* [39] proposed a new method of MRI reconstruction by utilizing a deep energy-based model. Another promising direction to address unsupervised MRI reconstruction is using score-based diffusion models. Song *et al.* [23] first presented a framework for score-based generative modeling based on stochastic differential equation (SDE). Later, Chung *et al.* [26] used the above idea to solve inverse problems in MRI, and have proven its effectiveness in accelerated MRI reconstruction.

### C. Score-based Generative Model with SDE

Score-based generative models have gained a lot of successes in generating realistic and diverse data recently. Score-based approaches define a forward diffusion process for transforming data to noise and generating data from noise by reversing the forward process. Recently, Song *et al.* [23] presented a SDE that transforms a complex data distribution to a known prior distribution by slowly injecting noise and a corresponding reverse-time SDE that transforms the prior distribution back into the data distribution by slowly removing the noise.

More specifically, we consider a diffusion process

$\{x(t)\}_{t=0}^T$  with  $x(t) \in \mathbb{R}^n$ , where  $t \in [0, T]$  is a continuous time variable and  $n$  denotes the image dimension. By choosing  $x(0) \sim p_0$  and  $x(T) \sim p_T$ ,  $p_0$  to be the data distribution and  $p_T$  to be the prior distribution, the diffusion process can be modeled as the solution of the following SDE:

$$dx = f(x, t)dt + g(t)dw \quad (3)$$

where  $f \in \mathbb{R}^n$  and  $g \in \mathbb{R}$  is the drift coefficient and the diffusion coefficient of  $x(t)$ , respectively. And  $w \in \mathbb{R}^n$  induces Brownian motion.

According to the reversibility of SDE, the reverse process of Eq. (4) can be expressed as another stochastic process:

$$dx = [f(x, t) - g(t)^2 \nabla_x \log p_t(x)]dt + g(t)d\bar{w} \quad (4)$$

where  $dt$  is the infinitesimal negative time step, and  $\bar{w}$  is a standard Wiener process for time flowing in reverse. The score term  $\nabla_x \log p_t(x)$  can be approximated by a learned time-dependent score model  $s_\theta(x, t)$ . The SDE is then solved by means of some solver procedure, providing the basis for score-based generative modeling with SDEs.

### III. METHOD

#### A. Skeleton of WKGM

In this work, we synergistically combine the generative network with conventional methods in our formulation, in which the unconstrained optimization problem can be transformed into:

$$\text{Min}_k \left\{ \|Mk - y\|_2^2 + \zeta R_{\text{Generative}}(k) + \lambda R_{\text{Conventional}}(k) \right\} \quad (5)$$

where  $\|Mk - y\|_2^2$  denotes forward consistency term, which enforces data consistency with acquired measurements  $y$ .  $\zeta$  and  $\lambda$  stand regularization parameters.  $R_{\text{Generative}}(k)$  is a k-space generative model that is able to achieve highly quality iterative reconstruction from the learned prior data distribution. The image reconstructed by the generative

network  $R_{\text{Generative}}(k)$  is used as a regularization term. The detailed introduction about the prior learning and reconstruction process of  $R_{\text{Generative}}(k)$  is presented in Section III. C and Section III. D. Furthermore, the reconstruction architecture embeds the additional regularization term  $R_{\text{Conventional}}(k)$ , which is determined by the traditional iterative algorithms (e.g., SAKE), efficiently modeling the recurrence of the iterative reconstruction stages. The additional regularization term  $R_{\text{Conventional}}(k)$  is incorporated into the reconstruction architecture based on  $R_{\text{Generative}}(k)$  in a complementary and harmonious way. Details of  $R_{\text{Conventional}}$  are given in Section III. E.

Fig. 1 intuitively shows the prior learning and reconstruction process of WKGM. In the prior learning stage, the complex-valued reference data are taken as the initial input of the training network. Subsequently, the weighting technology is enforced on each k-space input data, and the high-dimensional space strategy is imposed after the k-space weighting operation. Hence, we obtain a weighted high-dimensional tensor as the final input of the training network, where the real-value and imaginary-value components are concatenated along the channel dimension. Last, the score network is trained by learning the final composite k-space input data. For the reconstruction process, we use a PC sampler on the weighted input data to iteratively reconstruct the objects from the trained score network. The operation of removing the same weight is applied after PC sampling. In each iteration reconstruction step, the data consistency is simultaneously enforced to ensure that the output is consistent with the original k-space information. Moreover, the traditional k-space MRI algorithm (e.g., SAKE) is embedded to the reconstruction stage for better performance. Since WKGM is based on k-space domain, reconstruction in image domain is obtained by applying the inverse Fourier encoding. The final image is then obtained by the square root of the sum of squares (SOS) image.

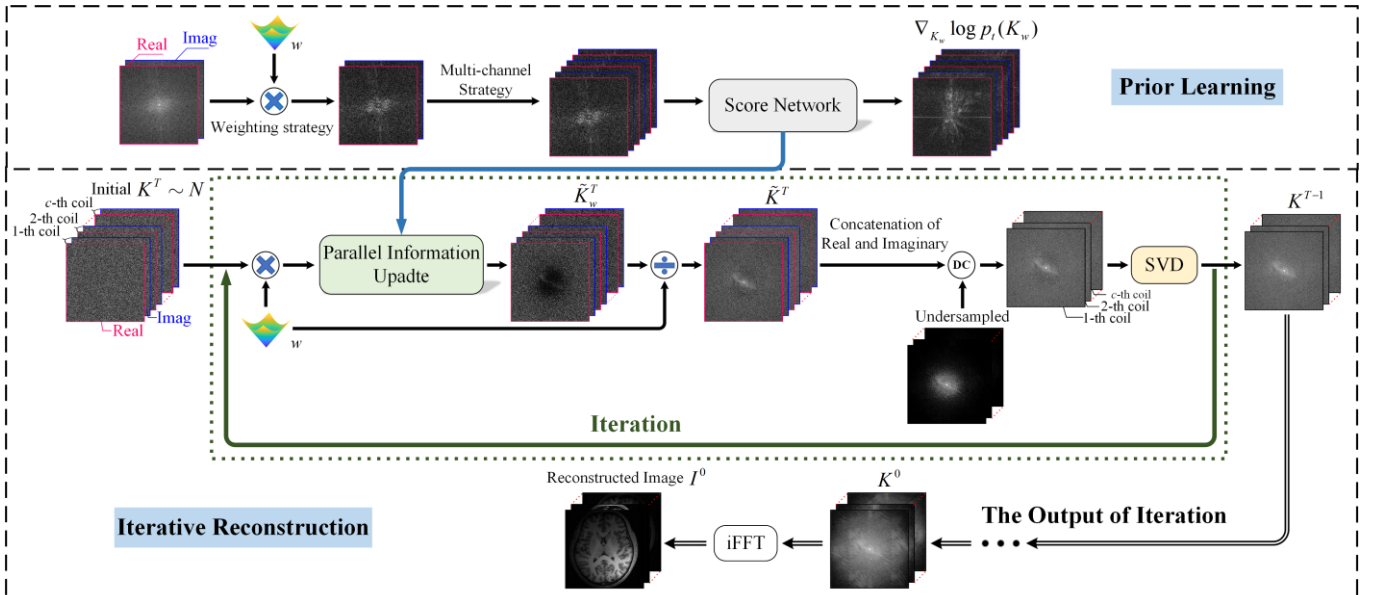


**Fig. 1.** Pipeline of the prior learning process and MRI reconstruction procedure in WKGM. Top line: Prior learning is conducted in weight-k-space domain at a single coil. Bottom line: PI reconstruction is conducted in iterative scheme that alternates between WKGM update and other traditional iterative methods.

#### B. Motivation of Weight-k-Space

In k-space, the low frequency and high frequency components are concentrated in the central and surrounding re-

gions, respectively. Since the range between low spatial frequency and high spatial frequency varies greatly, training  $R_{Generative}(k)$  directly on k-space domain is intractable. Inspired by the success of these works in [40]-[41], in this work, the weighting strategy is imposed on k-space input data to reduce the frequency range between high frequency and low frequency information. As shown in Fig. 2, the amplitude values of pixel locations in weighted k-space domain are much closer and homogeneous. Meanwhile, it can be noticed that the main component of signals in the image support is low-frequency information, thus image support can also be efficiently reduced by suppressing low-frequency information with the weighting technique. Also, using weighting strategy, the corresponding output is high-frequency as feature, which is sparser and consistent with the spirit of compressed sensing. As shown in Fig. 3, the weighting technology is applied to multi-channels k-space data for MRI reconstruction in this work. Using k-space weighting techniques on multi-channel data not only reduces frequency range of each coil image but also increases the correlation between coil images. We can therefore make better use of the similarity between coils to MRI reconstruction.

We apply k-space weighting technology on the input data, which can be represented as:

$$k_w = wk, \quad w = (r \cdot x_k^2 + r \cdot y_k^2)^p \quad (6)$$

where  $k$  denotes k-space input data of the training network,  $w$  represents weight matrix.  $k_w$  stands the weighted k-space input data.  $x_k$  and  $y_k$  are the count of frequency encoding lines and phase encoding lines, respectively.  $r$  and  $p$  stand two parameters for adjusting weight, where  $r$  sets the cutoff value and  $p$  determines the smoothness of the weight boundary.

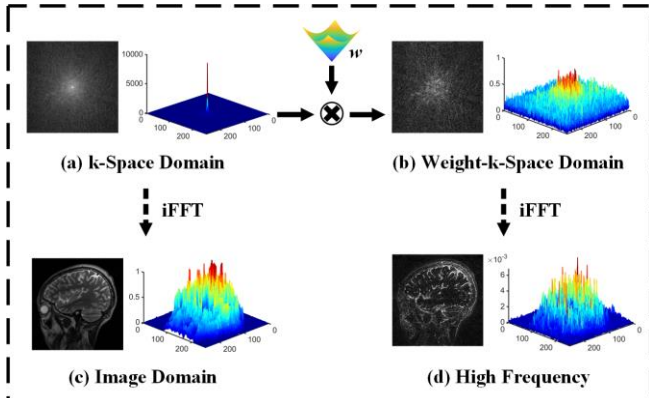


**Fig. 2.** Visual comparison of the amplitude values in image domain, and the corresponding k-space domain and weight-k-space domain. (a) The reference k-space data and its amplitude values. (b) The weight-k-space data and its amplitude values. (c) The image obtained by applying the inverse Fourier encoding on k-space data. (d) The image obtained by applying the inverse Fourier encoding on weight-k-space data.

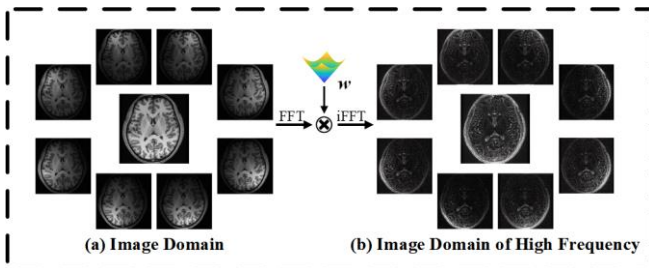


**Fig. 3.** Visual comparison of the amplitude values in image domain.

Quan *et al.* [25] elaborated that prior information learned from high-dimensional tensor can achieve more effective MRI reconstruction than low-dimensional counterpart. To generate network  $R_{Generative}(k)$  to with prior data information at high-dimensional manifold, avoiding difficulties for the accuracy in score estimation and sampling, we introduce a high-dimensional space embedding strategy to form high dimensional tensor, where the real and imaginary components are concatenated along the channel dimension. As shown in Fig. 4,  $K_w = \{[k_w^{re1}, k_w^{im1}], [k_w^{re2}, k_w^{im2}], [k_w^{re3}, k_w^{im3}]\}$  is a 6-channel high-dimensional tensor.  $[k_w^{re1}, k_w^{im1}]$  denotes the channel concatenation of real and imaginary components. Eq. (5) can be represented as:

$$\begin{aligned} & \text{Min}_k \left\{ \|Mk - y\|_2^2 + \zeta R_{Generative}(K_w) + \lambda R_{Conventional}(k) \right\} \\ & \text{s.t. } K_w = \{[k_w^{re1}, k_w^{im1}], [k_w^{re2}, k_w^{im2}], [k_w^{re3}, k_w^{im3}]\} \\ & \quad k_w = wk \end{aligned} \quad (7)$$

where the weighted and high-dimensional k-space data  $K_w$  is the final input data of the training network.

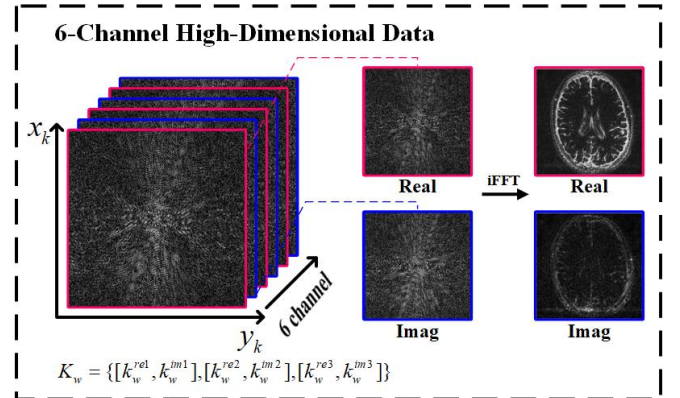


**Fig. 4.** Visualization of the 6-channel high-dimensional data  $K_w$ .

### C. Prior Learning in Weight-k-Space

With the introduction of deep learning, many studies incorporated convolutional neural networks into MRI reconstruction. In this study, we propose that  $R_{Generative}(K_w)$  is the scored-based generate network, which learns the prior data distribution from input data  $K_w$  to achieve high quality MRI reconstruction. In score-based approaches, the diffusion process progressively adds noise to transform the complex data distribution into a Gaussian noise distribution from which we can sample as shown in Fig. 5. Song *et al.* formalized this noising process as the forward SDE, as shown in Eq. (3). In our work, it can be reformulated as:

$$dK_w = f(K_w, t)dt + g(K_w)dw \quad (8)$$

The process of Eq. (8) is reversed to transform Gaussian noise into data for samples generation. The reverse-time SDE can be given by:

$$dK_w = [f(K_w, t) - g(t)^2 \nabla_{K_w} \log p_t(K_w)]dt + g(t)d\bar{w} \quad (9)$$

The reverse-time SDE requires the time-dependent score function  $\nabla_{K_w} \log p_t(K_w)$  to be known in advance. In practice, the score function  $\nabla_{K_w} \log p_t(K_w)$  is intractable. Fortunately, it can be estimated by training a time-dependent score network  $s_\theta(K_w(t), t)$  parameterized by  $\theta$ .  $s_\theta(K_w(t), t)$  can be trained by optimizing the following objective:

$$\theta^* = \arg \min_{\theta} \mathbb{E}_t \{ \lambda(t) \mathbb{E}_{K_w(0)} \mathbb{E}_{K_w(t)|K_w(0)} [ \|s_{\theta}(K_w(t), t) - \nabla_{K_w(t)} \log p_{0t}(K_w(t) | K_w(0))\|^2 ] \} \quad (10)$$

where  $\lambda(t): \mathbb{R} \rightarrow \mathbb{R}$  is a weighting function. Vincent *et al.* [42] demonstrated that the minimizer of that objective  $\theta^*$  will be such that  $s_{\theta}(K_w(t), t) \approx \nabla_{K_w} \log p_t(K_w)$ , which means that  $\nabla_{K_w} \log p_t(K_w)$  is known for all  $t$  by trained  $s_{\theta}(K_w(t), t)$ , allowing us to derive the reverse diffusion process of Eq. (9) and simulate it to sample.

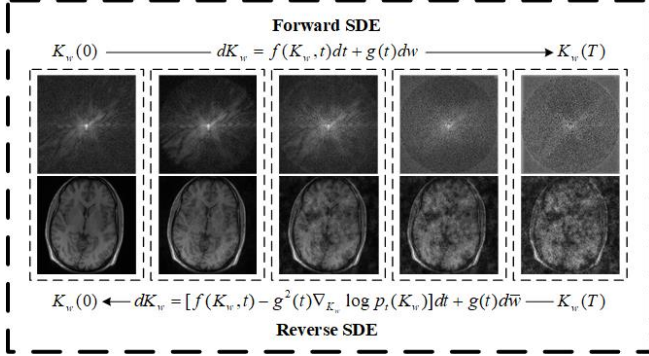


Fig. 5. Illustration of the forward and reverse processes of k-space data and the corresponding image. The forward process can be accomplished with a continuous-time SDE. The reverse time SDE can be solved by training a score network to estimate the score function  $\nabla_{K_w} \log p_t(K_w)$ .

#### D. PI Reconstruction of WKGM

In the inverse problem of reconstructing  $k$  from  $y$ , the question of interest is generating samples from the posterior distribution  $p(k|y)$ . It can be solved by converting it into the optimization problem:

$$\text{Min}_k \left\{ \|Mk - y\|_2^2 + \zeta R_{\text{Generative}}(K_w) \right\} \quad (11)$$

We elaborate the prior learning process of  $R_{\text{Generative}}(K_w)$  in Section III. C, the reconstruction process of  $R_{\text{Generative}}(K_w)$  is given as follows.

Once score network  $s_{\theta}(K_w(t), t)$  is trained, we insert it into Eq. (9) and solve the resulting reverse SDE to achieve MRI reconstruction:

$$dK_w = [f(K_w, t) - g(t)^2 s_{\theta}(K_w(t), t)]dt + g(t)d\bar{W} \quad (12)$$

To solve the reverse SDE, based on research by Song *et al.*, the PC sampler is introduced in this work, where Variance Exploding (VE) SDE solver is selected as the predictor, annealed Langevin dynamics (ALD) as the corrector to correct the solution of a numerical VE SDE solver, as shown in Eq. (13). We can therefore obtain the samples from the obtained prior distribution by solving the reverse SDE numerically. Among them, each unconditional sampling update step involves the operation of weighting and dividing with the same weight in solving VE SDE and ALD sampling.

$$\begin{aligned} \text{Predictor} : K_{w_i} &= (\sigma_{i+1}^2 - \sigma_i^2) s_{\theta}(K_{w_{i+1}}, \sigma_{i+1}) + \sqrt{\sigma_{i+1}^2 - \sigma_i^2} z \\ \text{Corrector} : K_{w_i} &= K_{w_{i+1}} + \varepsilon_i s_{\theta}(K_{w_{i+1}}, \sigma_{i+1}) + \sqrt{2\varepsilon_i} z \end{aligned} \quad (13)$$

where the initial solution  $K_{w_0}$  can be a total uniform noise or other predefined value.  $\varepsilon > 0$  is a step size,  $i$  is the total number of iterations, and  $z$  is a zero-mean Gaussian white noise with variance.

Note that we aim to sample from the  $p(k|y)$ , which can

be achieved by alternating between enforcing projection-based data consistency step at every reconstruction iteration and the unconditional samples update step. In data-consistency layer, weighted high-dimensional data  $K_w$  is transformed to the high-dimensional tensor  $K$  by removing the weight. And then  $K$  is replaced by the k-space data  $k$  after channel averaging operation. The data-consistency problem is solved via:

$$k(j) = \begin{cases} k^{\text{gen}}(j), & \text{if } j \notin \Omega \\ \frac{k^{\text{gen}}(j) + \lambda k^u(j)}{1 + \lambda}, & \text{if } j \in \Omega \end{cases} \quad (14)$$

where  $k^u$  is the undersampled k-space measurement,  $\lambda$  is a ratio of regularization parameter,  $\Omega$  denotes an index set of the acquired k-space samples.  $k^{\text{gen}}(j)$  represents an entry at index  $j$  in k-space. In the noiseless setting (i.e.,  $\lambda \rightarrow \infty$ ), we simply replace the  $j_{\text{th}}$  predicted coefficient by the original coefficient if it has been sampled. The image is reconstructed by applying the inverse of the Fourier encoding matrix  $I = F^{-1}k(j)$ . The final reconstruction is obtained by combining the channels through the SOS. It compactly represents the training and sampling process of WKGM by **Algorithm 1**.

#### Algorithm 1: WKGM

##### Training stage

**Setting:**  $r, p, w$

**1: Dataset:** Higher-dimensional k-space dataset

$$K_w = \{[k_w^{\text{re1}}, k_w^{\text{im1}}], [k_w^{\text{re2}}, k_w^{\text{im2}}], [k_w^{\text{re3}}, k_w^{\text{im3}}]\}, k_w = w \cdot k$$

**2: Output:** Trained  $S_{\theta}(K_w, \sigma)$

##### Reconstruction stage

**Setting:**  $N, M, w$

**1:**  $K_w^N \sim N(0, \sigma_T^2 \mathbf{1})$

**2: For**  $i = N-1$  to 0 **do (Outer loop)**

**3:**  $\tilde{K}_w^i \leftarrow \text{Predictor}(K_w^{i+1}, \sigma_i, \sigma_{i+1})$

**4:**  $\tilde{K}^i \leftarrow \tilde{K}_w^i / w$

**5: Update**  $\tilde{k}^i = \text{Mean}(\tilde{K}^i)$  and Eq. (14)

**6:**  $\tilde{k}_w^i = w \cdot \tilde{k}^i$

**7:**  $\tilde{K}_w^i \leftarrow \{[\tilde{k}_w^{\text{re1}}, \tilde{k}_w^{\text{im1}}], [\tilde{k}_w^{\text{re2}}, \tilde{k}_w^{\text{im2}}], [\tilde{k}_w^{\text{re3}}, \tilde{k}_w^{\text{im3}}]\}$

**8: For**  $j=1$  to  $M$  **do (Inner loop)**

**9:**  $\tilde{K}_w^{i,j} \leftarrow \text{Corrector}(K_w^{i,j-1}, \sigma_i, \varepsilon_i)$

**10:**  $\tilde{K}^{i,j} \leftarrow \tilde{K}_w^{i,j} / w$

**11: Update**  $\tilde{k}^{i,j} = \text{Mean}(\tilde{K}^{i,j})$  and Eq. (14)

**12:**  $\tilde{k}_w^i = w \cdot \tilde{k}^{i,j}$

**13:**  $\tilde{K}_w^{i,j} \leftarrow \{[\tilde{k}_w^{\text{re1}}, \tilde{k}_w^{\text{im1}}], [\tilde{k}_w^{\text{re2}}, \tilde{k}_w^{\text{im2}}], [\tilde{k}_w^{\text{re3}}, \tilde{k}_w^{\text{im3}}]\}$

**14: End For**

**15: End For**

**16:**  $k^{\text{rec}} \leftarrow \tilde{k}^0$

**17: Return**  $I_{\text{sos}} = \sqrt{\sum_{c=1}^C |(F^{-1}k_c^{\text{rec}})|^2}$

#### E. Combination with Traditional Algorithms

The proposed model WKGM is iterative. Hence, it offers flexibility for incorporating any traditional k-space domain algorithms into the whole reconstruction process. In this work, we combine WKGM with traditional algorithm SAKE

[8] by alternating iteration reconstruction to further improve MRI reconstruction performance. In other words, the additional regularization term  $R_{Conventional}(k)$  is determined by the traditional iterative algorithm SAKE.

SAKE is a calibrationless reconstruction algorithm forming the whole k-space data into a Hankel structured low-rank matrix to recover images from undersampled multi-channel data. Specifically, SAKE connects the multi-channel data in series and the connected data is reformulated as the shape of the Hankel matrix used for Cadzow's signal enhancement. This structured matrix has low rank nature due to the linear dependency of the multi-channel MRI data [43]-[44]. As a result, the extension to recovery of PI without a fully sampled calibration region can be formulated as a structured low rank matrix completion problem. The solution is obtained by a projection-onto-sets type algorithm with singular value thresholding, especially hard-thresholding [45]. The SAKE reconstruction is formulated as a constraint optimization, that is:

$$\begin{aligned} \text{Min}_k \|Mk - y\|_2^2 \\ \text{s.t. } \text{rank}(A) = a, k = H^+(A) \end{aligned} \quad (15)$$

where  $A$  denotes the low-rank data matrix and  $H^+$  is the pseudo-inverse operator. SAKE can easily incorporate additional a priori information. We can therefore combine SAKE with the proposed method WKGM. The optimization problem in Eq. (7) can be rewritten as follows:

$$\begin{aligned} \text{Min}_k \|Mk - y\|_2^2 + \zeta R_{Generative}(K_w) \\ \text{s.t. } \text{rank}(A) = a, k = H^+(A) \end{aligned} \quad (16)$$

That's consistent with Eq. (7). **Algorithm 2** exhibits the whole reconstruction procedure as follows:

---

**Algorithm 2: Reconstruction stage in svd-WKGM**

---

**Setting:**  $N, M, w$

- 1:  $K_w^N \sim N(0, \sigma_T^2 I)$
  - 2: **For**  $i = N - 1$  to  $0$  **do (Outer Loop)**
  - 3:   **Step 3- 7 in Algorithm 1**
  - 4:   **For**  $j = 1$  to  $M$  **do (Inner Loop)**
  - 5:     **Step 9-11 in Algorithm 1**
  - 6:      $A_k^j \leftarrow H(\tilde{k}^{i,j})$  (**Hankel Matrix**)
  - 7:      $[U, S, V] = \text{svd}(A_k^j)$  (**Perform SVD**)
  - 8:      $A_k^j \leftarrow USV^T$  (**Low-rank Matrix**)
  - 9:      $\tilde{k}^{i,j} \leftarrow H^T(A_k^j)$  and **Update** Eq. (14)
  - 10:    **Step 12-13 in Algorithm 1**
  - 11:    **End for**
  - 12: **End for**
  - 13: **Step 16-17 in Algorithm 1**
- 

## IV. EXPERIMENTS

### A. Experiment Setup

1) **Datasets:** The brain images are selected from *SIAT* dataset, which was provided by Shenzhen Institutes of Advanced Technology, the Chinese Academy of Science. Informed consents are obtained from the imaging subject in compliance with the institutional review board policy. The collected dataset consists of 500 2D complex-valued MR images with  $256 \times 256$  pixels. In details, MR images are acquired from a healthy volunteer on a 3.0T Siemens Trio Tim MRI scanner using the T2 weighted turbo spin echo sequence. Repetition time (TR)/echo time (TE) is

$6100/99$  ms, and field of view (FOV) is  $220 \times 220$  mm<sup>2</sup>. Besides, the voxel size is  $0.9 \times 0.9 \times 0.9$  mm<sup>3</sup>.

Aside from *SIAT* dataset, we conduct experiments on four in-vivo datasets to verify the reconstruction performance of WKGM. First, a brain image from a healthy volunteer was acquired with a T1-weighted, 3D spoiled gradient echo sequence. Scan parameters were set to TE, 8 ms, TR, 17.6 ms, and flip angle, 20°. Imaging parameters were chosen such that FOV is  $20\text{cm} \times 20\text{cm} \times 20\text{cm}$  with a matrix size of  $200 \times 200$  for an isotropic 1 mm<sup>3</sup> resolution. A single axial slice was selected from this data set and was used throughout the experiments. The scan was performed on a 1.5T MRI scanner (GE, Waukesha, Wisconsin, USA) using an 8-channel receive-only head coil. Second, the *T1 GE Brain* includes 8-channel complex-valued MR images with size of  $256 \times 256$ . The MR images are acquired by 3.0T Siemens. The FOV is  $220 \times 220$  mm<sup>2</sup>, and TR/TE is 700/11 ms. Also, 12-channel *T2 transversal brain* MR images with size of  $256 \times 256$  are acquired with 3.0 T Siemens, whose FOV is  $220 \times 220$  mm<sup>2</sup> and TR/TE is 5000/91 ms. For the *knee* dataset, the raw data was acquired from 3D fast-spin-echo (FSE) sequence with proton density weighting included fat saturation comparison by a 3.0T whole body MR system (Discovery MR 750, DV22.0, GE Healthcare, Milwaukee, WI, USA). The TR/TE is 1550/25 ms. There were 320 slices in total, and the thickness of each slice was 0.6 mm. FOV is  $160 \times 128$  mm<sup>2</sup> and the size of acquisition matrix is  $320 \times 256$ .

2) **Parameter Setting:** In this subsection, parameter settings in the proposed algorithm are discussed. The batch size is set to 2 and Adam optimizer with  $\beta_1=0.9$  and  $\beta_2=0.999$  is utilized to optimize the network. For noise variance schedule, we fix  $\sigma_{\max}=1$ ,  $\sigma_{\min}=0.01$  and  $r=0.075$ . For all the algorithms, we use  $N=1000, M=1$  iterations. For the other parameters, we follow the settings in the work of Song *et al* [23]. The training and testing experiments are performed with 2 NVIDIA TITAN GPUs, 12 GB.

### 3) Evaluation Metrics:

To quantitatively evaluate the performance of the various reconstruction models, we choose two classic metrics, namely peak signal to noise ratio (PSNR), and structural similarity index measure (SSIM). The PSNR describes the relationship of the maximum possible power of a signal with the power of noise corruption, and the SSIM is used to measure the similarity between the original image and reconstructed images. For the convenience of reproducibility, the source code and some representative results are available at: <https://github.com/yqx7150/WKGM>.

### B. Reconstruction Comparisons

To evaluate the reconstruction performance, we compare the proposed WKGM and svd-WKGM methods with other state-of-the-art algorithms, including ESPiRiT [6], SAKE [8], P-LORAKS [9], as well as LINDBERG [46] and EBMRec [39]. Moreover, we conduct the experiments under various sampling patterns (e.g., Poisson, 2D Partial Fourier and Random sampling) and different acceleration factors (i.e., 4×, 6×, 8×, and 10× factors of acceleration).

Fig. 6 depicts the qualitative reconstruction results of WKGM and svd-WKGM, ESPiRiT, P-LORAKS and SAKE, along with their corresponding 5× magnified residual images. We conduct the experiments on *T1-weighted* image under Poisson sampling patterns with acceleration factors  $R=4$ ,

8 and 2D Partial Fourier sampling patterns with acceleration factors  $R=3, 6$ , respectively. From Fig. 6, we can observe that there are significant residual artifacts and amplified noise that exist in the results obtained by ESPIRiT, SAKE, and P-LORAKS. Nevertheless, the reconstructed image of svd-WKGM preserves more small textural details and has the least noise relative to the reference image. Furthermore, the difference images at the second row of Fig. 6 illustrate that svd-WKGM achieves the lowest reconstruction errors. In ESPIRiT and P-LORAKS, there remains much more

noise in their reconstruction results. In SAKE, the overall reconstruction errors are higher than those from svd-WKGM. Table I presents the quantitative comparisons of these methods. The image reconstructed by svd-WKGM has the largest PSNR and SSIM values than the other reconstructions under different sampling strategies and acceleration factors, indicating the effectiveness of the proposed method. These observations correspond well with the qualitative analysis shown in Fig. 6.

TABLE I  
PSNR AND SSIM COMPARISON WITH STATE-OF-THE-ART PI METHODS UNDER DIFFERENT SAMPLING PATTERNS WITH VARYING ACCELERATE FACTORS.

(a)	ESPIRiT	SAKE	P-LORAKS	WKGM	svd-WKGM
Poisson $R=4$	33.97/0.862	35.71/0.916	34.62/0.896	35.13/0.905	<b>36.15/0.923</b>
Poisson $R=8$	32.04/0.802	32.92/0.851	32.02/0.860	31.88/0.788	<b>34.03/0.881</b>
(b)	ESPIRiT	SAKE	P-LORAKS	WKGM	svd-WKGM
Partial 2D $R=3$	30.12/0.838	30.87/0.904	28.95/0.848	30.21/0.894	<b>31.05/0.909</b>
Partial 2D $R=6$	29.68/0.810	30.18/0.862	28.74/0.829	28.37/0.826	<b>30.35/0.865</b>

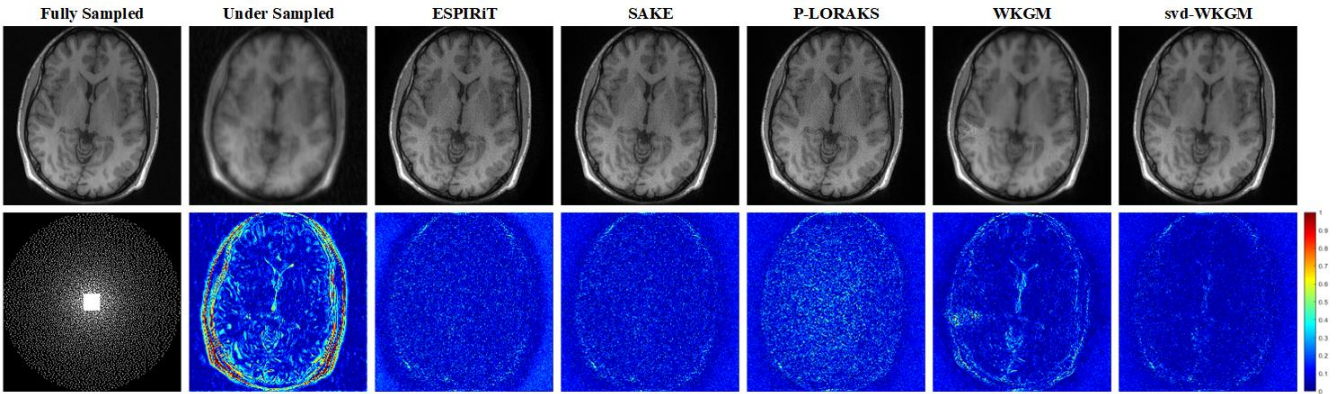


Fig. 6. Complex-valued PI reconstruction results at  $R=8$  using Poisson sampling with 8 coils. From left to right: Fully sampled, Undersampled, reconstruction by ESPIRiT, SAKE, P-LORAKS, WKGM and svd-WKGM. The intensity of residual maps is five times magnified.

Figs. 7 and 8 intuitively illustrate the representative reconstructions of the proposed methods and competitive methods, such as ESPIRiT, LINDBERG, EBMRec and SAKE. For  $T1$  GE Brain dataset, we use Random 2D sampling patterns, with acceleration factors of 4 and 6, respectively. For  $T2$  Transversal Brain dataset, the Poisson sampling patterns with acceleration factors of 4 and 10 are applied to test. In line with previous results, svd-WKGM provides better image quality with noise-like artifacts effectively suppressed compared with competitive results. The second line in Figs. 7 and 8 depicts the reconstruction errors of svd-WKGM, WKGM, and compared methods. It indicates that ESPIRiT, EBMRec, and SAKE show noticeable noise-like residuals associated with the vulnerability of noise at high acceleration compared to the reference images. LINDBERG exhibits spatial blurring, which is effectively mitigated by svd-WKGM reconstruction. It can also be seen

that svd-WKGM can generate superior performance, even at an extremely high acceleration factor, as shown in Fig. 8. Correspondingly, Table II tabulates the numerical results of the proposed methods and other comparison methods in terms of PSNR and SSIM metrics. In most cases, both of test indicators of WKGM are higher than ESPIRiT, LINDBERG and EBMRec, followed by SAKE. However, svd-WKGM still outperforms the competitive method SAKE.

It can also be observed that svd-WKGM consistently outperforms other competitive methods under various sampling strategies. svd-WKGM reduces sampling-specific effects, i.e., the difference between sampling schemes becomes less severe. These experiments demonstrate that the proposed model can be well generalized to various sampling patterns with different acceleration factors.

TABLE II  
PSNR AND SSIM COMPARISON WITH STATE-OF-THE-ART PI METHODS UNDER DIFFERENT SAMPLING PATTERNS WITH VARYING ACCELERATE FACTORS.

$T1$ GE Brain	ESPIRiT	LINDBERG	EBMRec	SAKE	WKGM	svd-WKGM
Random 2D $R=4$	39.08/0.933	38.98/0.961	40.17/0.968	41.54/0.952	40.45/0.968	<b>43.83/0.970</b>
Random 2D $R=6$	36.01/0.921	35.16/0.958	36.55/0.952	38.09/0.932	37.14/0.957	<b>39.94/0.960</b>
$T2$ Transversal Brain	ESPIRiT	LINDBERG	EBMRec	SAKE	WKGM	svd-WKGM
Poisson $R=4$	31.74/0.819	32.87/0.901	33.19/0.915	33.91/0.896	33.35/0.907	<b>34.95/0.916</b>
Poisson $R=10$	28.95/0.798	26.17/0.822	29.59/0.839	29.75/0.823	29.17/0.823	<b>31.69/0.841</b>

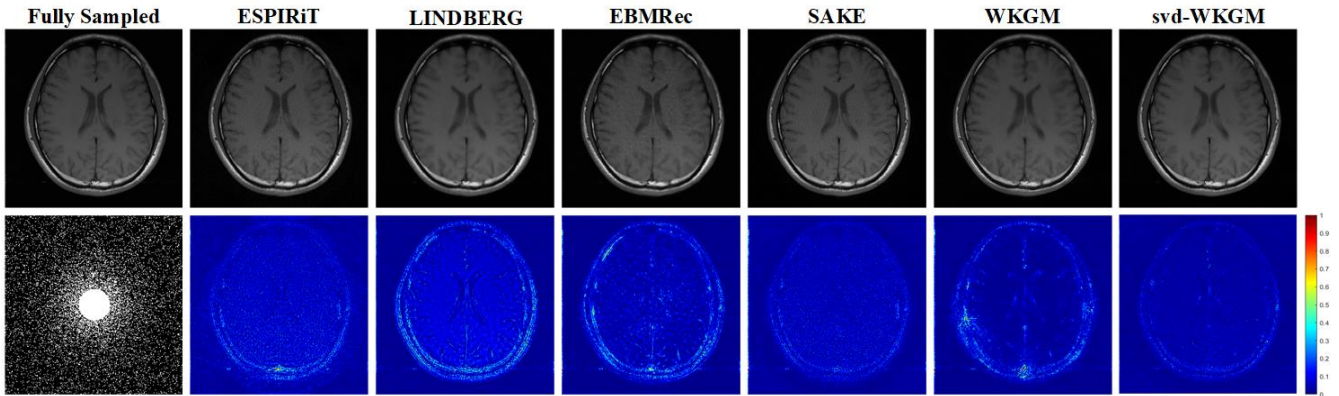


Fig. 7. PI reconstruction results by ESPIRiT, LINDBERG, EBMRec, SAKE and svd-WKGM on *T1 GE Brain* image at  $R=6$  using a 2D Random disk sampling mask. The intensity of residual maps is five times magnified.

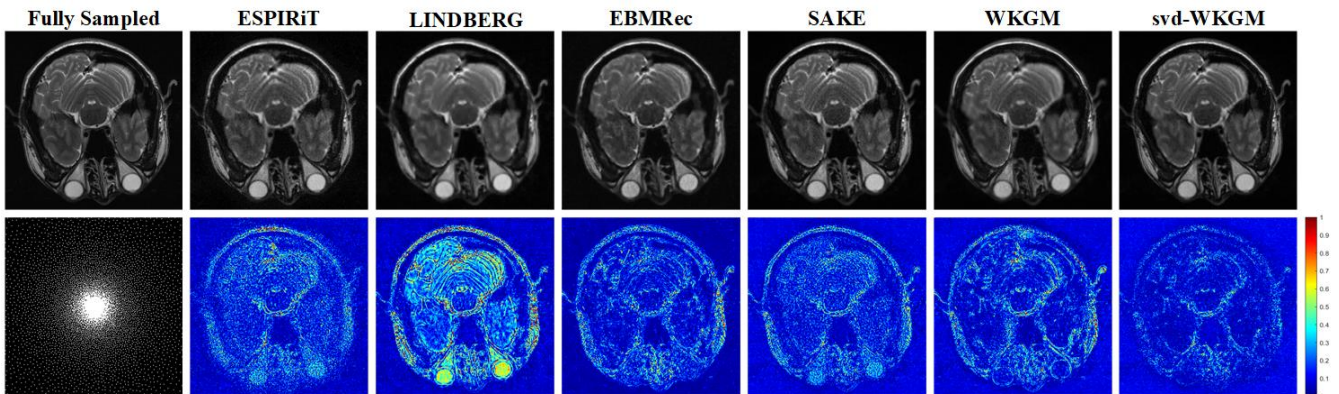


Fig. 8. PI reconstruction results by ESPIRiT, LINDBERG, EBMRec, SAKE, WKGM and svd-WKGM on *T2 Transversal Brain* image at  $R=10$  using 2D Poisson disk sampling mask. The intensity of residual maps is five times magnify.

Table III lists the quantitative comparisons of the proposed method svd-WKGM, respectively, with zero-filled and csgm-mri-langevin [27] methods. The experimental results are obtained on 16-channel *T2-weighted brain* image under Vertical and Horizontal sampling masks with acceleration factor  $R=3$ . Compared to csgm-mri-langevin method, the reconstruction performance of svd-WKGM improves with significantly higher PSNR and SSIM values under two different types of sampling patterns. Specifically, the PSNR value of the reconstructed image by svd-WKGM increases up to 1 dB compared to csgm-mri-langevin. Fig. 9 depicts the qualitative results of svd-WKGM and competition methods, it can be seen that svd-WKGM has much lower errors with finer reconstruction details and much more edge information compared to csgm-mri-langevin. In general, svd-WKGM produces visually more convincing and accurate reconstruction with much higher PSNR and SSIM values.

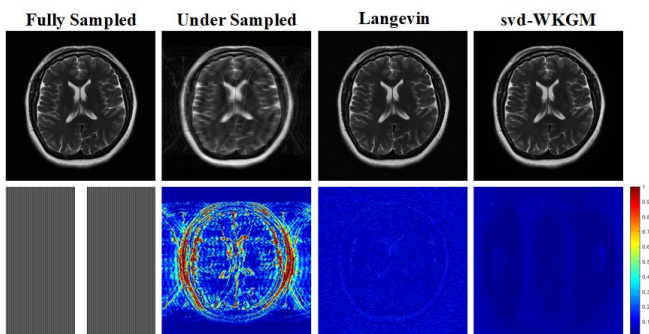


Fig. 9. PI reconstruction results by zero-filled, csgm-mri-langevin, and svd-WKGM on *T2-weighted brain* image at  $R=3$  vertical sampling mask. The intensity of residual maps is five times magnify.

TABLE III  
PSNR AND SSIM COMPARISON WITH CSGM-MRI-LANGEVIN METHOD UNDER DIFFERENT PATTERNS AT  $R=3$ .

<i>T2 Brain</i> $384 \times 384 \times 16$	Zero-filled	csgm-mri-langevin	svd-WKGM
Vertical $R=3$	23.51/0.693	37.47/0.940	<b>38.42/0.953</b>
Horizontal $R=3$	26.28/0.759	38.44/0.950	<b>39.51/0.960</b>

To further assess the reconstruction performance of svd-WKGM, a comparison with k-space deep learning [16] is conducted in this experiment. The quantitative analysis of the reconstructed image in TABLE IV, shows PSNR and SSIM values of the reconstructed knee image using Cartesian trajectory at  $R=3$  and Poisson trajectory at  $R=6$ . As can be seen from the numerical results, the experimental result of k-space deep learning under  $R=3$  Cartesian sampling trajectory has slightly higher PSNR and SSIM values than svd-WKGM. It is reasonable because k-space deep learning is an end-to-end learning reconstruction method that requires training labels, while svd-WKGM is completely unsupervised.

Nevertheless, under Poisson sampling strategy with acceleration factor  $R=6$ , svd-WKGM reconstructs image with higher PSNR and SSIM values compared to k-space deep learning method. Additionally, the qualitative evaluation further confirms the quantitative performance improvements. Based on the reconstructions and errors residual images as shown in Fig. 10, it can be concluded that svd-WKGM is superior to k-space deep learning in terms of overall reconstruction quality and structure details reconstruction. Svd-WKGM provides significant advantages for high acceleration factors, with significantly improved reconstruction quality.



TABLE IV  
PSNR AND SSIM COMPARISON WITH K-SPACE DEEP LEARNING METHOD UNDER DIFFERENT SAMPLING PATTERNS WITH VARYING ACCELERATE FACTORS ON 8-COILS KNEE DATA.

Cartesian $R=3$	Zero-filled	k-space deep learning	svd-WKGM
100 <sup>th</sup> Slice	31.91/0.748	<b>35.35/0.813</b>	34.46/0.790
16 <sup>th</sup> Slice	31.52/0.749	<b>35.99/0.836</b>	33.88/0.805
Poisson $R=6$	Zero-filled	k-space deep learning	svd-WKGM
100 <sup>th</sup> Slice	23.02/0.690	30.96/0.767	<b>31.70/0.810</b>
16 <sup>th</sup> Slice	20.48/0.643	28.99/0.793	<b>29.81/0.832</b>

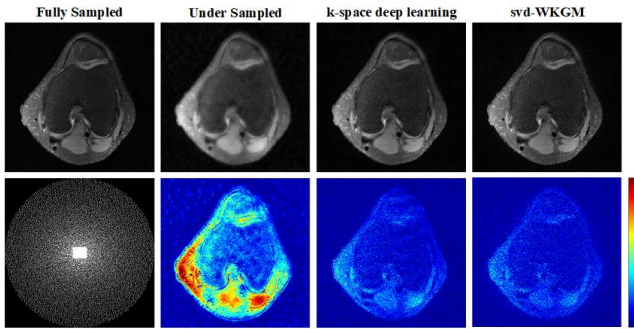


Fig. 10. PI reconstruction results by zero-filled, k-space deep learning, and svd-WKGM on 16<sup>th</sup> slice of eight coils knee k-space data at  $R=6$  using Poisson sampling mask. The intensity of residual maps is four times magnify.

### C. Convergence Analysis and Computational Costs

In this section, we experimentally investigate the convergence of WKGM and svd-WKGM in terms of quantitative metric PSNR with respect to the number of iteration reconstruction. We randomly select an example of reconstructing the brain image using 2D Poisson sampling pattern with acceleration factor  $R=3$ . As shown in Fig. 11, both the PSNR curve of WKGM and svd-WKGM rise rapidly as iteration increases and then approximately converge at a high PSNR level. Meanwhile, the PSNR curve of svd-WKGM ascends faster at early iterations and first converges to a stable point with the better numerical results than WKGM. For the computational complexity of the proposed method, it is concluded that the computational cost can be reduced by reducing the iteration number of the inner loop.

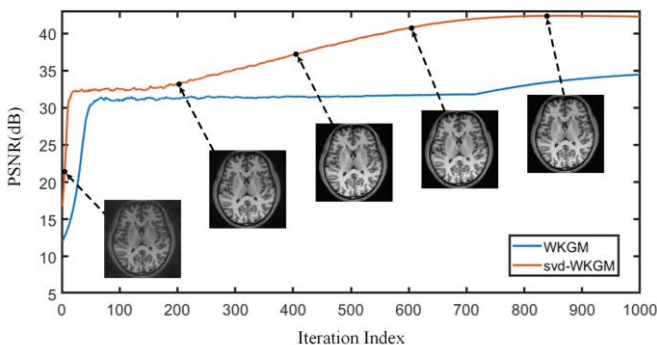


Fig. 11. Convergence curves of WKGM and svd-WKGM in terms of PSNR versus the iteration number when reconstructing the brain image from 1/3 sampled data under 2D Poisson sampling pattern.

### D. Ablation Study

To demonstrate the model generalization capability and robustness, i.e., to verify our hypothesis that the proposed model can be trained on an arbitrary coil, which can be applied to the reconstruction of any coils without much per-

formance loss, we perform an ablation study for PI reconstruction on 12 coils *SIAT* image using Radial 2D sampling pattern with acceleration factors  $R=3.3$  and 5. Fig. 12 and Table V show the qualitative and quantitative comparisons of the models trained on different coils (e.g., 1-th, 11-th and single coil). It can be found that the gap in reconstruction performance of the different coils trained models stays fairly small and constant. Furthermore, the model trained by single coil maintains the best result.

TABLE V  
PSNR AND SSIM COMPARISON OF DIFFERENT TRAINING MODEL UNDER DIFFERENT SAMPLING PATTERNS WITH VARYING ACCELERATE FACTORS ON 12 COILS *SIAT* DATA.

WKGM	1 <sup>st</sup> Coil	11 <sup>th</sup> Coil	Single Coil
Radial 2D $R=3.3$	34.33/0.920	34.34/0.922	34.32/0.921
Radial 2D $R=5$	31.05/0.906	31.59/0.904	31.09/0.902

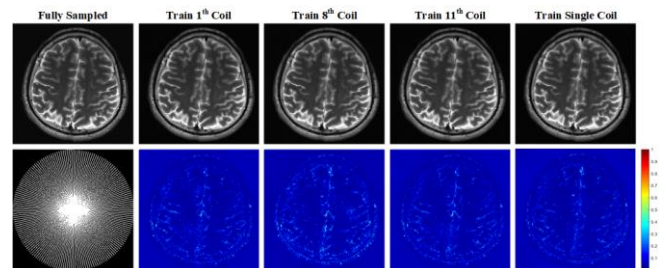


Fig. 12. PI reconstruction results of models trained using different coil images. From left to right: 1st-coil model, 8th-coil model, 11th-coil model and single coil model.

We evaluate the impact of different values of weight parameters  $r$  and  $p$  on WKGM reconstruction. Table VI reports the quantitative PSNR and SSIM results of the *T1 GE Brain* image under  $R=6$  Poisson sampling pattern and the corresponding frequency range of the image data. The original frequency range of *T1 GE Brain* image is 3820.8. From Table VI, one can observe that weight embedding strategy results in a significant reduction of frequency range and different values of weight parameters  $r$  and  $p$  result in different numerical results. We can therefore conclude that the appropriate selection of weight parameters  $r$  and  $p$  plays an especially important role in image reconstruction quality by the proposed model.

TABLE VI  
PSNR AND SSIM RESULTS OF DIFFERENT WEIGHT PARAMETER VALUES UNDER  $R=6$  POISSON SAMPLING MASK AND CORRESPONDING FREQUENCY RANGE.

WKGM	$p=0.4$	$p=0.5$	$p=0.6$
$r=1 \times 10^{-2}$	<b>38.47/0.966</b>	38.36/ <b>0.971</b>	32.24/0.874
$r=1.5 \times 10^{-2}$	37.50/0.940	<b>38.39/0.973</b>	34.13/0.936
$r=2 \times 10^{-2}$	35.65/0.935	<b>38.54/0.972</b>	36.20/0.963
frequency range after weighting	$p=0.4$	$p=0.5$	$p=0.6$
$r=1 \times 10^{-2}$	2.24	0.39	0.07
$r=1.5 \times 10^{-2}$	3.09	0.58	0.11
$r=2 \times 10^{-2}$	3.89	0.78	0.15

To demonstrate the superior performance of high-dimensional formulation strategy, we visualize the reconstruction results of the models trained on different channel data in Fig. 13. All results are obtained with Cartesian 1

D acquisition trajectories with acceleration factors  $R=3$ , 6.7 on *TI GE Brain* image. From the reconstruction results and corresponding error maps, it can be seen that models trained on 6 and 8-channel data obtain better reconstruction performance and lower reconstruction errors than reconstruction results of 2 and 4-channel counterparts. There is little difference between the reconstruction result of 6-channel and 8-channel models, which is also indicated by the variations of quantitative metrics. Considering that model trained on 8-channel data need much more computation than model trained on 6-channel data, the 6-dimensional space strategy is applied in all the experiments.

TABLE VII

PSNR AND SSIM VALUES OF MODELS TRAINED ON DIFFERENT CHANNELS DATA UNDER  $R=3$ , 6.7 CARTESIAN 1D SAMPLING PATTERN.

WKGM	2ch	4ch	6ch	8ch
Cartesian $R=3$	34.87/0.953	35.14/0.947	35.73/0.954	<b>35.95/0.954</b>
Cartesian $R=6.7$	28.59/0.895	29.56/0.901	30.74/0.904	<b>30.79/0.900</b>

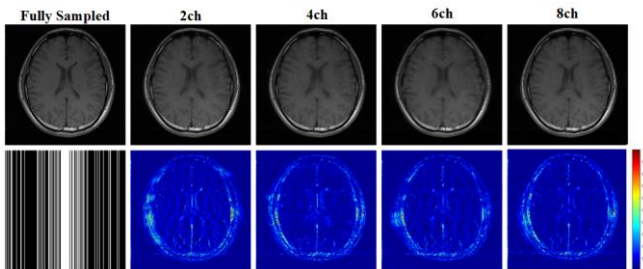


Fig. 13. PI reconstruction results of models trained on different channels data with  $R=3$  Cartesian sampling pattern. From left to right: Zero-filled, 2-channel model, 4-channel model, 6-channel model, and 8-channel model.

## V. CONCLUSION

This work proposed a weighted k-space generative model (WKGM) for multi-channel MRI reconstruction. The proposed WKGM applied a generative network and a weighting strategy to accelerate MRI reconstruction, and incorporated traditional methods in a harmonious way to improve PI reconstruction quality. Experiment results verified that the proposed methods WKGM and svd-WKGM can produce better reconstruction performance under different sampling patterns with large acceleration factors, keeping higher PSNR and SSIM values compared to other state-of-the-art methods. More traditional methods will be exploited in the future study to efficiently validate the flexibility of the proposed method.

## VI. REFERENCE

- [1] D. K. Sodickson, and W. J. Manning, "Simultaneous acquisition of spatial harmonics (SMASH): Fast imaging with radiofrequency coil arrays," *Magn. eason. Med.*, vol. 38, no. 4, pp. 591-603, 1997.
- [2] K. P. Pruessmann, M. Weiger, M. B. Scheidegger, and P. Boesiger, "SENSE: Sensitivity encoding for fast MRI," *Magn. eason. Med.*, vol. 42, no. 5, pp. 952-962, 1999.
- [3] M. A. Griswold, P. M. Jakob, R. M. Heidemann, M. Nittka, V. Jellus, J. Wang, B. Kiefer, and A. Haase, "Generalized autocalibrating partially parallel acquisitions (GRAPPA)," *Magn. eason. Med.*, vol. 47, no. 6, pp. 1202-1210, 2002.
- [4] M. Lustig, and J. Pauly, "SPIRiT: iterative self-consistent parallel imaging reconstruction from arbitrary k-space," *Magn. eason. Med.*, vol. 64, no. 2, pp. 457-471, 2010.
- [5] C. Liu, J. Zhang, and M. E. Moseley, "Auto-calibrated parallel imaging reconstruction for arbitrary trajectories using k-space sparse matrices (kSPA)," *IEEE Trans. Med. Imag.*, vol. 29, no. 3, pp. 950-959, 2010.

- [6] M. Uecker, P. Lai, M. J. Murphy, P. Virtue, M. Elad, J. M. Pauly, S. S. Vasanawala, and M. Lustig, "ESPIRiT-an eigenvalue approach to autocalibrating parallel MRI: where SENSE meets GRAPPA," *Magn. eason. Med.*, vol. 71, no. 3, pp. 990-1001, 2014.
- [7] A. Majumdar, and R. K. Ward, "Calibration-less multi-coil MR image reconstruction," *Magn. eason. Imag.*, vol. 30, no. 7, pp. 1032-1045, 2012.
- [8] P. J. Shin, P. E. Larson, M. A. Ohliger, M. Elad, J. M. Pauly, D. B. Vigneron, and M. Lustig, "Calibrationless parallel imaging reconstruction based on structured low-rank matrix completion," *Magn. eason. Med.*, vol. 72, no. 4, pp. 959-970, 2014.
- [9] J. P. Haldar, and J. Zhuo, "P-LORAKS: Low-rank modeling of local k-space neighborhoods with parallel imaging data," *Magn. eason. Med.*, vol. 75, no. 4, pp. 1499-1514, 2016.
- [10] D. Lee, K. H. Jin, E. Y. Kim, S. H. Park, and J. C. Ye, "Acceleration of MR parameter mapping using annihilating filter-based low rank hankel matrix (ALPHA)," *Magn. eason. Med.*, vol. 76, no. 6, pp. 1848-1864, 2016.
- [11] K. Hammernik, T. Klatzer, E. Kobler, M. P. Recht, D. K. Sodickson, T. Pock, and F. Knoll, "Learning a variational network for reconstruction of accelerated MRI data," *Magn. eason. Med.*, vol. 79, no. 6, pp. 3055-3071, 2018.
- [12] J. Schlemper, J. Caballero, J. V. Hajnal, A. N. Price, and D. Rueckert, "A deep cascade of convolutional neural networks for dynamic MR image reconstruction," *IEEE Trans. Med. Imag.*, vol. 37, no. 2, pp. 491-503, 2018.
- [13] H. K. Aggarwal, M. P. Mani, and M. Jacob, "MoDL: Model-based deep learning architecture for inverse problems," *IEEE Trans. Med. Imag.*, vol. 38, no. 2, pp. 394-405, 2019.
- [14] J. Duan, J. Schlemper, C. Qin, C. Ouyang, W. Bai, C. Biffi, G. Bello, B. Statton, D. P. O'Regan, and D. Rueckert, "VS-Net, Variable splitting network for accelerated parallel MRI reconstruction," *Int. Conf. Med. Image Comput. Comput.-Assist. Intervent.*, pp. 713-722, 2019.
- [15] Y. Liu, Q. Liu, M. Zhang, Q. Yang, S. Wang, and D. Liang, "IFR-Net: Iterative feature refinement network for compressed sensing MRI," *IEEE Trans. Comput. Imag.*, vol. 6, pp. 434-446, Nov. 2019.
- [16] Y. Han, L. Sunwoo, and J. C. Ye, "k-Space deep learning for accelerated MRI," *IEEE Trans. Med. Imag.*, vol. 39, no. 2, pp. 377-386, 2019.
- [17] I. J. Goodfellow, J. Pouget-Abadie, M. Mirza, B. Xu, D. Warde-Farley, S. Ozair, A. Courville, and Y. Bengio, "Generative adversarial nets," *Adv. Neural Inf. Process. Syst.*, vol. 27, 2014.
- [18] P. Vincent, "A connection between score matching and denoising autoencoders," *Neural Comput.*, vol. 23, no. 7, pp. 1661-1674, 2011.
- [19] Y. Song, and S. Ermon, "Generative modeling by estimating gradients of the data distribution," *Proc. Adv. Neural Inf. Process. Syst.*, pp. 11895-11907, 2019.
- [20] A. Hyvärinen and P. Dayan, "Estimation of non-normalized statistical models by score matching," *J. Mach. Learn. Res.*, vol. 6, no. 4, 2005.
- [21] J. Sohl-Dickstein, E. Weiss, N. Maheswaranathan, and S. Ganguli, "Deep unsupervised learning using nonequilibrium thermodynamics," *Int. Conf. on Mach. Learn.*, pp. 2256-2265, 2015.
- [22] J. Ho, A. Jain, and P. Abbeel, "Dennoising diffusion probabilistic models," *Adv. Neural Inf. Process. Syst.*, vol. 33, 2020.
- [23] Y. Song, J. Sohl-Dickstein, D. P. Kingma, A. Kumar, S. Ermon, and B. Poole, "Score-based generative modeling through stochastic differential equations," *arXiv preprint arXiv:2011.13456*, 2020.
- [24] Y. Song, L. Shen, L. Xing, and S. Ermon, "Solving inverse problems in medical imaging with score-based generative models," *arXiv preprint arXiv:2111.08005*, 2021.
- [25] C. Quan, J. Zhou, Y. Zhu, Y. Chen, S. Wang, D. Liang, and Q. Liu, "Homotopic gradients of generative density priors for MR image reconstruction," *IEEE Trans. Med. Imag.*, vol. 40, no. 12, pp. 3265-3278, 2021.
- [26] H. Chung, and J. C. Yea, "Score-based diffusion models for accelerated MRI," *arXiv preprint arXiv:2110.05243*, 2021.
- [27] A. Jalal, M. Arvinte, Daras G, E. Price, A. Dimakis, and J. Tamir, "Robust compressed sensing MRI with deep generative priors," *Adv. Neural Inf. Process. Syst.*, vol. 34, 2021.
- [28] Y. Xie, and Q. Li, "Measurement-conditioned denoising diffusion probabilistic model for under-sampled medical image reconstruction," *arXiv preprint arXiv:2203.03623*, 2022.
- [29] J. Haldar, "Low-rank modeling of local k-space neighborhoods (LORAKS) for constrained MRI," *IEEE Trans. Med. Imag.*, vol. 33, no. 3, pp. 668-681, 2014.
- [30] J. Y. Cheng, F. Chen, M. T. Alley, J. M. Pauly, and S. S. Vasanawala, "Highly scalable image reconstruction using deep neural networks with bandpass filtering," *arXiv preprint arXiv:1805.03300*, 2018.
- [31] M. Akçakaya, S. Moeller, S. Weingärtner, and K. Uğurbil, "Scan-specific robust artificial-neural-networks for k-space interpolation (RAKI) reconstruction: Database-free deep learning for fast imaging," *Magn. eason. Med.*, vol. 81, no. 1, pp. 439-453, 2019.
- [32] T. H. Kim, P. Garg, and J. P. Haldar, "LORAKI: Autocalibrated re-

- current neural networks for autoregressive MRI reconstruction in k-space,” *arXiv preprint arXiv:1904.09390*, 2019.
- [33] Y. Arefeen, O. Beker, J. Cho, H. Yu, E. Adalsteinsson, and B. Bilgic, “Scan-specific artifact reduction in k-space (SPARK) neural networks synergize with physics-based reconstruction to accelerate MRI,” *Magn. Reson. Med.*, vol. 87, no. 2, pp. 764-780, 2022.
- [34] K. C. Tezcan, C. F. Baumgartner, R. Luechinger, K. P. Pruessmann, and E. Konukoglu, “MR image reconstruction using deep density priors,” *IEEE Trans. Med. Imag.*, vol. 38, pp. 1633-1642, 2018.
- [35] Q. Liu, Q. Yang, H. Cheng, S. Wang, M. Zhang, and D. Liang, “Highly undersampled magnetic resonance imaging reconstruction using autoencoding priors,” *Magn. Reson. Med.*, vol. 83, no. 1, pp. 322-336, 2020.
- [36] A. Bora, A. Jalal, E. Price, and A. G. Dimakis, “Compressed sensing using generative models,” *Int. Conf. on Mach. Learn.*, pp. 537-546, 2017.
- [37] G. Luo, N. Zhao, W. Jiang, E.S. Hui, and C. Peng, “MRI reconstruction using deep Bayesian estimation,” *Magn. Reson. Med.*, vol. 84, no. 4, pp. 2246-2261, 2020.
- [38] V. A. Kelkar, S. Bhadra, and M. A. Anastasio, “Compressible latent-space invertible networks for generative model-constrained image reconstruction,” *IEEE Trans. Compu. Imag.*, vol. 7, pp. 209-223, 2021.
- [39] Y. Guan, Z. Tu, S. Wang, Q. Liu, Y. Wang, and D. Liang, “MRI reconstruction using deep energy-based model,” *arXiv preprint arXiv:2109.03237*, 2021.
- [40] K. H. Jin, D. Lee, and J. C. Ye, “A general framework for compressed sensing and parallel MRI using annihilating filter based low-rank hankel matrix,” *IEEE Trans. Compu. Imag.*, vol. 2, no. 4, pp. 480-495, 2016.
- [41] F. Huang, Y. Li, S. Vijayakumar, S. Hertel, and G. R. Duensing, “High-Pass GRAPPA: An image support reduction technique for improved partially parallel imaging,” *Magn. Reson. Med.*, vol. 59, no. 3, pp. 642-649, 2008.
- [42] P. Vincent, “A connection between score matching and denoising autoencoders,” *Neural Comput.*, vol. 23, no. 7, pp. 1661-1674, 2011.
- [43] J. Zhang, C. Liu, and M. E. Moseley, “Parallel reconstruction using null operators,” *Magn. Reson. Med.*, vol. 66, no. 5, pp. 1241-1253, 2011.
- [44] M. Lustig, M. Elad, and J. M. Pauly, “Calibrationless parallel imaging reconstruction by structured low-rank matrix completion,” *In Proceedings of the 18th Annual Meeting of ISMRM, Stockholm*, pp. 2870, 2010.
- [45] J. A. Cadzow, “Signal enhancement—a composite property mapping algorithm,” *IEEE Trans. Acoust., Speech, and Signal. Process.*, vol. 36, no. 1, pp. 49-62, 1988.
- [46] S. Wang, S. Tan, Y. Gao, Q. Liu, L. Ying, T. Xiao, Y. Liu, X. Liu, H. Zheng, and D. Liang, “Learning joint-sparse codes for calibration-free parallel MR imaging,” *IEEE Trans. Med. Imag.*, vol. 37, no. 1, pp. 251-261, 2017.